

# A spatial-temporal analysis approach for flutter predictions using decoupled and fully-coupled methods

H. M. Phan\*

*Department of Engineering Science, University of Oxford, Oxford OX2 0ES, United Kingdom*

---

## Abstract

Accurate and efficient numerical predictions of flutter is essential for the turbomachinery industry. The decoupled method has been the main workhorse of the industry for decades thanks to its low computational resources required. However, there arises the need for an innovative propulsion architecture and a lightweight material, which hinders the accuracy and effectiveness of the decoupled method. Hence, the use of fully-coupled methods for flutter predictions has been steadily increasing. Despite more demanding computational resources needed to perform the fully-coupled simulations, the large amount of data generated in the time-domain is not often used efficiently. Typically the aeroelastic stability is judged in a straightforward manner using the logarithmic decrement. Although this global parameter is useful to compare the aeroelastic stability among configurations, it yields almost no meaningful understanding of the physical vibration mechanisms. In the present paper, a spatial-temporal analysis approach based on the Hilbert transform is proposed. It can work well with the non-linear non-stationary data typically generated from the time-domain fully-coupled solutions. In addition, the Hilbert transform-based analysis approach is designed to be consistent with the conventional energy method when the newly developed method is applied to the decouple simulation data. The Hilbert transform-based approach is applied to three computational examples, each with a particular aeroelastic flow mechanisms of interest (i.e. tip clearance, laminar separation bubble, stall). The new approach has been shown to effectively elucidate the associated vibration mechanisms using the decomposition method in space and time.

© 2017 Elsevier Inc. All rights reserved.

*Keywords:* Turbomachinery; Flutter; Aerodynamic Damping; Hilbert Transform; Fluid-structure interaction

---

## 1. Introduction

Flutter is a self-excited aeroelastic instability phenomenon that endangers the structural integrity and leads to failures of turbomachinery blades. Accurate and efficient predictions of blade flutter is crucial in the engine development and the certification campaign. Modern computational turbomachinery flutter predictions are built upon the two most important modelling bases, namely the monochromatic travelling wave concept [1] and the energy method [2]. The first assumption dictates that the blades in the same row would vibrate at a same frequency and a constant inter-blade phase angle corresponding to the least stable condition. The second assumption simplifies the flutter prediction process into a decoupled manner such that the aerodynamic forces are assumed to have a negligible effect on the structural responses. Thus, the in-vacuo mode shape and frequency can be obtained separately and used as an input to the Computational Fluid Dynamics (CFD) codes. The energy method adopts the concept of aerodynamic damping to determine the flutter susceptibility. When the aerodynamic damping is positive, the blade vibration energy dissipates to the surrounding medium and the blade would be stable. Vice versa, when the aerodynamic damping is negative, the blade absorbs energy from the surrounding medium and the blade would be unstable. Since its

---

\* Corresponding author.

*E-mail address:* hien.phan@eng.ox.ac.uk

introduction, the energy method has become the most common method for turbomachinery flutter predictions thanks to its simplicity. Its associated spanwise integration capability is also compatible with the section-by-section design procedures [3], though direct 3D simulations with energy method have now been popular [4-6].

Although the establishment of the monochromatic travelling wave is generally accepted except for mistuning [7], the accuracy of the decoupled energy method is highly dependent on the degree of fluid-structure coupling. For blades made of titanium or nickel-based alloys, its high mass ratio and high stiffness-to-weight ratio enables the successful application of the decoupled energy method. However, with the search for an innovative propulsion architecture and lightweight material, the decoupling assumption is likely to be violated. Unfortunately, these innovative changes are usually more prone to aeroelastic stabilities as the boundary is pushed. Extensive efforts are being carried out by research groups worldwide to improve understanding of the aeroelastic characteristics of the new propulsion architectures. In the next decade, one of the most promising propulsion configuration is the ultra-high-bypass-ratio (UHBR) low-speed fan stage. However, the UHBR low-speed fan technology will also be more susceptible to stall-driven instability as the compressor is operated predominantly on the flat part of the characteristic curves [8]. Regarding the same UHBR fan, Rendu et al. [9] proposed a linear decomposition method to investigate the physical mechanisms of choke flutter. Using this decomposition analysis approach, the aeroelastic characteristics of the UHBR fan at choke flutter condition are found to be driven by regressive waves generated by the vibration of the blade downstream section. Being investigated at NASA, the boundary layer ingestion (BLI) is another promising propulsion technology. The central idea is that the engines would be embedded on the airframe such that the airframe boundary layer can be ingested and re-energized by the engines. This potentially can result to the theoretical fuel burn reduction up to 10%. However, the fan is subject to constant unsteady inlet distortion, which poses a significant challenge for maintaining the aeroelastic stability [10]. Another example is the counter-rotating open rotor (CROR) with a high fuel saving potential due to the removal of residual swirl from the downstream flow. While the aerodynamics and aeroacoustics performance of this technology has been studied extensively, its aeroelastic stability is not studied often despite the increased susceptibility to flutter. Stapelfeldt et al. [11] studied the flutter behavior of the CROR rig at the take-off condition, which observed the minimum damping at low advance ratios accompanied by highly three-dimensional features on the suction surface.

Even for the current state-of-the-art propulsion technology, the low mass ratio configuration can have a strong nonlinear aeroelastic effect. Sadeghi and Liu [12] showed a discrepancy of the predicted flutter boundary between the decoupled and the fully-coupled methods. Carstens and Belz [13] reported a nonlinear flutter at transonic flow condition using the fully-coupled method. Chahine et al. [14] investigated flutter of the transonic fan rotor across a range of mass ratio and stiffness. They concluded that the decoupled and fully-coupled methods are in good agreement across a large range of structural conditions. Nevertheless, the prediction discrepancy can be up to 27.3% at a combined low mass ratio and low stiffness condition. As a result, the use of fully-coupled methods becomes more popular especially for fundamental studies. Vahdati et al. [15] used the fully-coupled approach to explain the stall and acoustic flutter mechanisms of the wide-chord fan blade. Gan et al. [16] adopted the fully-coupled fluid-structure interaction method to investigate the non-synchronous vibration of a compressor rotor. Phan and He [17, 18] used the fully-coupled method to elucidate the vibration mechanisms of the structurally and aerodynamically mistuned cascade.

Although the computational cost of the fully-coupled method is high, their generated simulation data are much less used compared to the decoupled method. Most studies adopting the fully-coupled methods would use logarithmic decrement (log-dec) to judge the aeroelastic stability in a straightforward manner: the blade is stable if log-dec is positive and unstable if log-dec is negative. However, log-dec is a global parameter, which is hardly useful to understand the physical vibration mechanism at local regions. In addition, the classical peak-based log-dec has been shown to be less accurate and not desirable for certain nonlinear configurations [19]. To overcome this problem, the time-varying characteristics are used by some researchers to estimate the nonlinear system [20, 21], although these methods do not provide information of the locally spatial characteristics.

With the background and issues of interest as introduced so far, there arises the need to make use of the rich data obtained from the time-domain fully-coupled simulations to investigate the local vibration mechanism effects. This analysis approach needs to be able to deal with the non-linear and non-stationary data from the fully-coupled simulations. In addition, applying this approach to the decoupled simulation data should yield a consistent conclusion to the conventional flutter prediction methods. Therefore we propose an analysis approach based on the Hilbert transform, which in its original form has been attracting considerable attention for the analyses of the non-linear and

non-stationary signals. Bowles et al. [22] proposed a Hilbert transform-based approach to study the oscillating helicopter rotor blade subject to stall flutter. They found that the cycle-integrated aerodynamic damping coefficient masks the physics of the aeroelastic stability mechanisms. Malik and Raveh [23] extended the aforementioned Hilbert transform approach to compute the aerodynamic damping distribution along the chord. The method was applied to study the pitching airfoil, which found negative aerodynamic damping near the leading and trailing edge regions. Jacobson et al. [24] also realized the need for high-fidelity aeroelastic design tools and compared various damping identification methods available. The Hilbert transform-based approach was also among the investigated methods, however its use to extract the amplitude envelope made it similar to the conventional log-dec method. One other thing can be observed that those methods existing in the literature mostly focus on the data set obtained from the forced vibration problems, where the imposed periodic vibration is a-priori known.

In the current paper, we propose a rather different Hilbert transform-based approach that is formulated to deal with time-domain data obtained from fully-coupled simulations of the free vibration. Nevertheless, if this method is applied to the forced vibration or decoupled simulation data, it would yield consistent conclusions with the typical decoupled flutter prediction method. The proposed method is an analysis approach that would reveal the spatial-temporal vibration mechanisms of the investigated airfoil.

In the following sections, we will firstly present the conventional flutter prediction methods for both decoupled and fully-coupled simulation approach. Then, the formulation for the Hilbert transform-based approach is introduced. Finally, the proposed approach will be applied to various examples to show how this approach can enhance our understanding on the turbomachinery flutter mechanisms of different contributing factors.

## Nomenclature

$C$	blade chord
HT	Hilbert transform
SS	suction surface
PS	pressure surface
$\Xi$	aerodynamic damping
$q$	vibration amplitude
$p$	pressure
$W$	aerodynamic work
Re	real part
Im	imaginary part
$C_p$	steady pressure coefficient; $C_p = (p - p_2)/(p_{01} - p_2)$
$\omega$	angular frequency
$k$	reduced frequency; $k = \omega C / V_{ref}$
$p_{01}$	inlet total pressure
$p_2$	outlet static pressure
$V_{ref}$	reference isentropic exit velocity; $V_{ref} = \sqrt{2(p_{01} - p_2)/\rho}$
$x$	axial chordwise distance

## Superscripts

$\sim$	Hilbert transform operator
$\wedge$	amplitude

## 2. Conventional flutter prediction methods

### 2.1. Decoupled simulation – Energy method

In the decoupled simulation approach, a specific vibration mode shape and frequency of interest are imposed. Consider a sinusoidal blade vibration, its local displacement is:

$$D = \hat{q} \sin(\omega t) \quad (1)$$

The vibrational velocity is its time derivative:

$$V = \omega \hat{q} \cos(\omega t) \quad (2)$$

The unsteady pressure perturbation induced by the blade vibration is characterized by the vibration frequency:

$$p = \hat{p} \sin(\omega t + \psi) \quad (3)$$

The aerodynamic work done is the integral of the unsteady pressure perturbation and the vibrational velocity:

$$W = \int_t^{t+T} \int_s p \mathbf{n} \cdot \mathbf{u} ds dt \quad (4)$$

Integrating the aerodynamic work done during a vibration period gives:

$$W = \int_s \pi \hat{p} \hat{q} \cdot \sin(\psi) ds \quad (5)$$

The spanwise-averaged aerodynamic damping is calculated by integrating along the blade chord at each spanwise layer:

$$\mathcal{E}_c = \frac{1}{c} \int_s \frac{-\pi \hat{p} \hat{q} \cdot \sin(\psi) ds}{(p_{01} - p_2) \widehat{q_{tip}}^2} = \frac{1}{c} \int_s \frac{-\pi \widehat{C_p} \hat{q} \cdot \sin(\psi) ds}{\widehat{q_{tip}}^2} \quad (6)$$

where  $p_{01} - p_2$  is the dynamic head;  $\widehat{C_p} = \hat{p} / (p_{01} - p_2)$ .

The overall aerodynamic damping is calculated by integrating along the blade span:

$$\mathcal{E} = \frac{1}{h} \int_0^h \mathcal{E}_c dz \quad (7)$$

### 2.2. Fully-coupled method – Logarithmic decrement

In the fully-coupled simulation approach, the vibration mode shape and frequency are part of the solution. An initial disturbance is imposed on the airfoil and the solution is time-marched until reaching full coupling. The log-dec is calculated from the peaks of the time-domain vibration history:

$$\log \text{dec} = \frac{1}{n} \ln \frac{\hat{q}(t_0)}{\hat{q}(t_n)} \quad (8)$$

where  $n$  is the number of vibration cycles considered.

The damping factor can be calculated from the logarithmic decrement:

$$\zeta = \frac{1}{\sqrt{1+(2\pi/\log \text{dec})^2}} \quad (9)$$

For a small value of damping factor, it is approximated as:

$$\zeta = \frac{\log \text{dec}}{2\pi} \quad (10)$$

With the assumption of linear flow behavior, the damping factor is calculated as:

$$\zeta = \frac{-W}{2\pi\omega^2\hat{q}^2} \quad (11)$$

where  $\omega$  is the oscillating frequency.

For comparison with the uncoupled method, the damping ratio can be converted to the equivalent aerodynamic damping:

$$\mathcal{E} = \log \text{dec} \times \frac{\omega^2}{(P_{01}-P_2)} \quad (12)$$

### 3. Hilbert transform-based approach for spatial-temporal analysis

#### 3.1. Fundamental of Hilbert transform

The integral Hilbert transform (HT) of a time-domain signal  $y(t)$ , denoted as  $\tilde{y}(t)$ , is defined as:

$$\tilde{y}(t) \equiv \text{HT}[y(t)] = -\frac{1}{\pi} P.V. \int_{-\infty}^{\infty} \frac{y(\tau)}{\tau-t} d\tau \quad (13)$$

where HT is the Hilbert operator and P.V. is the Cauchy principal value.

A complex analytic signal can be formed whose real part is the original signal and the imaginary part is the Hilbert transform of the real part:

$$Y(t) = y(t) + i \cdot \tilde{y}(t) \quad (14)$$

The analytic signal can be represented in a trigonometric or exponential form:

$$Y(t) = |Y(t)|[\cos\phi(t) + i \cdot \sin\phi(t)] = A(t)e^{i\phi(t)} \quad (15)$$

where  $A(t)$  is the instantaneous amplitude

$$A(t) = \sqrt{y(t)^2 + \tilde{y}(t)^2} \quad (16)$$

and  $\phi(t)$  is the instantaneous phase angle

$$\phi(t) = \arctan \frac{\tilde{y}(t)}{y(t)} \quad (17)$$

For a more complete review on the basic of the Hilbert transform and its use in mechanical vibration analyses, one is recommended to read the tutorial in Ref. [25].

### 3.2. Hilbert transform-based flutter analysis

Starting from the equation of motion:

$$m\ddot{q} + c\dot{q} + kq = f \quad (18)$$

where  $m$  is modal mass,  $c = \bar{c}e^{i\gamma_c}$  is modal damping,  $k = \bar{k}e^{i\gamma_k}$  is modal stiffness, and  $f$  is modal aerodynamic damping force. Note that the mass and stiffness retains its dependency on time, which can account for nonlinear responses to the blade motion. Substituting the polar form of the mass and stiffness to the equation of motion yields:

$$m\ddot{q} + \bar{c}e^{i\gamma_c}\dot{q} + \bar{k}e^{i\gamma_k}q = f \quad (19)$$

In order to make use of the Hilbert transform-based approach, each term in Eq. 19 is replaced by its HT analytic representation:

$$m\ddot{Q} + \bar{c}e^{i\gamma_c}\dot{Q} + \bar{k}e^{i\gamma_k}Q = F \quad (20)$$

where  $Q(t) = q(t) + i \cdot \text{HT}[q(t)] = \hat{q}e^{i\omega t}$

$$F(t) = f(t) + i \cdot \text{HT}[f(t)] = \hat{f}e^{i\phi(t)}$$

Substituting  $Q$  and its derivatives to Eq. 20 yields:

$$-m\omega^2\hat{q} + \bar{c}i\omega\hat{q}(\cos\gamma_c + i \cdot \sin\gamma_c) + \bar{k}\hat{q}(\cos\gamma_k + i \cdot \sin\gamma_k) = \hat{f}e^{i\phi}e^{-i\omega t} = \hat{f}e^{i\psi} \quad (21)$$

where  $\psi = \phi - \omega t$

Equating the imaginary part of Eq. 21 gives:

$$\bar{c}\omega\hat{q}\cos(\gamma_c) + \bar{k}\hat{q}\sin(\gamma_k) = \overline{c_{eq}}\omega\hat{q} = \hat{f}\sin\psi \quad (22)$$

where  $\overline{c_{eq}} = \bar{c}\cos\gamma_c + \bar{k}\sin\gamma_k/\omega$  is the equivalent viscous damping. It can be seen that the equivalent viscous damping contains both the real part (cosine term) of the damping term and the imaginary part (sine term) of the stiffness term. If the nonlinearity of the damping and stiffness terms is neglected, those terms will be constant and the equivalent viscous damping  $\overline{c_{eq}} = c$ .

From the equivalent viscous damping, the instantaneous damping work can be calculated as:

$$\begin{aligned} W_d(t) &= \overline{c_{eq}}Re(\dot{Q})^2 \\ &= \frac{\hat{f}\sin\psi}{\omega\hat{q}} \times [-\omega^2\hat{q}^2\cos(\omega t)^2] \\ &= -\hat{f}\omega\hat{q} \cdot \sin\psi \cdot \cos(\omega t)^2 \end{aligned} \quad (23)$$

The instantaneous damping can be calculated as:

$$\mathcal{E}(t) = \frac{W_d(t)}{(P_{01}-P_2)\overline{q_{tip}}^2} \quad (24)$$

It can be seen that the instantaneous aerodynamic damping is time-dependent. The time-averaged damping can be found from any time interval:

$$\bar{\mathcal{E}}_{avg} = \int_{t_1}^{t_2} \mathcal{E}(t) dt \quad (25)$$

For practical calculation of the aerodynamic damping, the amplitudes and phases can be calculated from the original signals and their respective HTs:

$$\hat{f} = \sqrt{f^2 + \tilde{f}^2} \quad (26)$$

$$\hat{q} = \sqrt{q^2 + \tilde{q}^2} \quad (27)$$

$$\psi = \arctan\left(\frac{q\tilde{f} - \tilde{q}f}{qf + \tilde{q}\tilde{f}}\right) \quad (28)$$

More interestingly, if the vibration is periodic as in the decoupled method, it can be shown (in Appendix A) that the Hilbert transform-based aerodynamic damping can be simplified to an expression consistent to the conventional energy method:

$$\bar{\mathcal{E}}_{avg} = \frac{1}{c} \int_s \frac{-\pi \hat{p} \hat{q} \cdot \sin(\psi) ds}{(P_{01} - P_2) \bar{q}_{tip}^2} \quad (29)$$

## 4. Computational methodology

### 4.1. Numerical method

On the fluid side, the unsteady Navier-Stokes equations are solved iteratively in an implicit manner:

$$\begin{aligned} \frac{\partial \rho}{\partial t} + \nabla \cdot (\rho \mathbf{U}) &= 0 \\ \frac{\partial (\rho \mathbf{U})}{\partial t} + \nabla \cdot (\rho \mathbf{U} \otimes \mathbf{U}) &= -\nabla p + \nabla \cdot \boldsymbol{\tau} \\ \frac{\partial (\rho H)}{\partial t} - \frac{\partial p}{\partial t} + \nabla \cdot (\rho \mathbf{U} H) &= \nabla \cdot (\lambda \nabla T) + \nabla \cdot (\mathbf{U} \cdot \boldsymbol{\tau}) \end{aligned} \quad (30)$$

The governing equations represent the conservation of mass, momentum, and energy at each instantaneous time level. In order to close the equations, a turbulence model has to be used. In this work, both fully-turbulent and transitional Shear Stress Transport (SST) model will be investigated.

On the structure side, the rigid body equations of motion are solved separately for bending and torsion vibration mode:

$$\begin{aligned} \frac{dP}{dt} &= F_{aero} - k_{bending}(x - x_{COM}) \\ \frac{d\Pi}{dt} &= M_{aero} - k_{torsion}(\theta - \theta_{COM}) \end{aligned} \quad (31)$$

where  $P$  is linear momentum,  $\Pi$  is angular momentum.  $F_{aero}$  and  $M_{aero}$  denotes the aerodynamic force and moment acting on the blade, respectively. Similarly,  $k_{bending}$  and  $k_{torsion}$  represent the stiffness in the respective degree of freedom.

For a decoupled simulation, a mode shape with fixed oscillation amplitude is used to drive the blade movement. The mesh motion is therefore known a-priori. At each time instant, the mesh motion equation will be solved separately from the flow equations, thus it is known as decoupled simulation. On the other hand, for a fully-coupled simulation, the instantaneous oscillation amplitude is not known a-priori. It is an implicit result from the two-way balance of flow and rigid body equations such that the dependencies between the fluid and the body are converged within a time step.

#### 4.2. Boundary conditions

At the inlet, total pressure, total temperature, and flow angle are specified. At the outlet, static pressure is used. The solid walls including the blade, hub, and shroud surfaces are modelled as an adiabatic no-slip wall. At two outermost interfaces, a direct periodic condition is applied.

#### 4.3. Meshing

ICEM is used to make the unstructured hexahedral mesh for the numerical simulations. The near-wall boundary layer region is resolved with 40 elements in the normal direction to ensure that  $y^+ < 1$ . For three-dimensional simulations with tip gap, the tip region has about 20 cells in the radial direction to resolve the tip leakage flow.

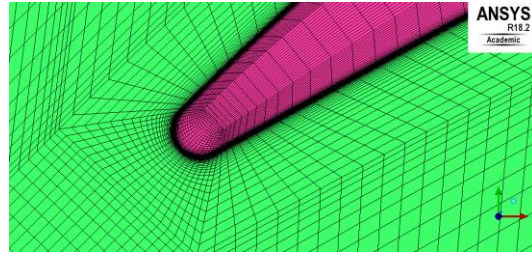


**Fig. 1.** Mesh resolution in the tip gap region.

### 5. Test case

In the present work, a control-diffusion (CD) type compressor blade profile is adopted. The blade geometry is the representative of modern blading designs. It has been used as the aeroelastic test cases for both experiment and computation purposes [6, 26]. The experimental results presented in the current study for validation purposes are acquired from the oscillating cascade test. The experiment was conducted at a Reynolds number  $Re = 1.95 \times 10^5$ . This test case has various important features that are of interest of turbomachinery designers. Firstly, it has a mid-chord laminar bubble-type separation with subsequent transition to turbulent flow. For compressors, the laminar separation-transition is essential in aerodynamic performance, which received great attention in the past [27, 28]. For turbines, the extensive use of highly loaded low-pressure turbine in modern design leads to significant interest in the interaction between separation bubble and the incoming wakes [29, 30]. Secondly, this test case has substantial measurement data near the tip region. With extensive use of three-dimensional flow features in modern design, this is suitable to study the aerodynamic/aeroelastic effects of tip leakage flow.

### 6. Verification and validation

#### 6.1. Verification of Hilbert transform against analytical Theodorsen's model

To verify the Hilbert transform calculation, we shall adopt the analytical solution of the Theodorsen's model for the airfoil undergoing harmonic pitching. The configuration is the same as that used in the literature [22]. The moment induced by the oscillation is given as:

$$C_m = \frac{\pi k^2 \alpha_1}{2} \left( \frac{3}{8} - \frac{i}{k} \right) (\cos \omega t + i \sin \omega t) \quad (32)$$

The analytical amplitude and phase of the aerodynamic moment are:

$$A = \frac{\pi k \alpha_1}{2} \sqrt{1 + \frac{9}{64} k^2}$$

$$\psi = \arctan \left( \frac{-8}{3k} \right) \quad (33)$$

The harmonic oscillation is  $\alpha = 6 + 8\cos(\omega t)$  and  $k = 0.1$ . The real and imaginary parts of the pitching moment are denoted as  $\text{Re}(C_m)$  and  $\text{Im}(C_m)$  respectively. The in-phase and quadrature pitching moment are given as in Ref. 22 and Ref. 25:

$$\overline{Cm_R} = \alpha \cdot \widetilde{C_m} - \tilde{\alpha} \cdot C_m$$

$$\overline{Cm_I} = \alpha \cdot C_m + \tilde{\alpha} \cdot \widetilde{C_m} \quad (34)$$

The analytical in-phase and quadrature pitching moment coefficients can be shown to be expressed as:

$$\overline{Cm_R} = 3\pi k^2 \alpha_1 / 16$$

$$\overline{Cm_I} = -\pi k \alpha_1 / 2 \quad (35)$$

Figure 2 shows the comparison between the computed and analytical results for the pitching moment coefficients. One should bear in mind that the Hilbert transform-based computational results are time-dependent such that each discrete marker in Fig. 2 represents an instantaneous solution. On the other hand, the analytical in-phase and quadrature pitching moment coefficients, represented by a continuous line in Fig. 2, are constant (see Eq. 35). For this simple verification case, the temporal fluctuation of the in-phase and quadrature moment coefficients are negligible. Thus, the Hilbert transform-based  $\overline{Cm_R}$  and  $\overline{Cm_I}$  are almost constant across the harmonic oscillation.

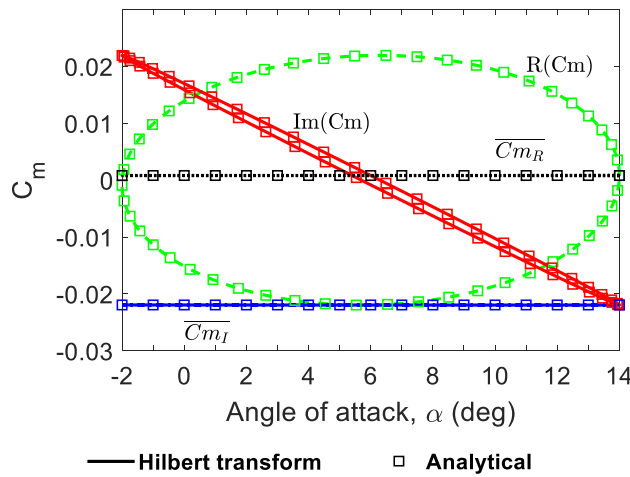


Fig. 2. Verification of numerical Hilbert transform against analytical solution of Theodorsen's pitching moment.

From Fig. 2, the Hilbert transform-based and analytical pitching moment coefficients have been shown to agree well with each other. Next, we will examine the comparison between the global variables of interest. Table 1 shows the comparison of amplitude, phase, and aerodynamic damping. Note that the aerodynamic damping here is computed following the literature [22] for direct comparison purposes. It can be seen that the Hilbert transform approach in the present work has been implemented correctly.

Table 1. Comparison of analytical Theodorsen's model and numerical Hilbert transform results.

	Analytical	Numerical [18]	Numerical (present)
Amplitude $A/\alpha_1$	0.15719	0.157	0.15719
Phase $\psi$	-1.53331	-1.53	-1.53331
Aerodynamic damping $\Xi$	0.15708	0.16	0.15708

## 6.2. Steady flow validation

The steady aerodynamic characteristics of the chosen compressor airfoil will be validated against the experiment. The laminar bubble separation is observed on the blade suction surface in the experiment at a low Reynolds number testing condition. In the previous computational study by the author [6], it was shown that using the two-equation  $\gamma$ - $\theta$  transition correlation coupled with the RANS SST model [31] is able to predict the formation of separation bubble. Figure 3 compares the steady pressure distribution at mid-span and near-tip to that predicted by the present CFD model. It is noted that a proper inlet boundary layer profile has to be used for the improved near-tip predictions [6]. From Fig. 3, it can be seen the near-tip loading is significantly reduced. This is attributed to the presence of passage vortex near the casing region, which highlights the strong three-dimensional effects in this test case.

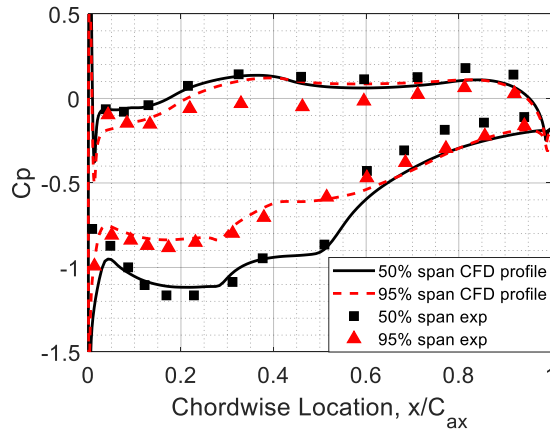


Fig. 3. Steady pressure distributions at mid-span and near-tip.

## 7. Applications of the Hilbert transform-based analysis approach

In the main part of the present study, we will apply the proposed Hilbert transform-based analysis approach on different computational test cases with a specific physical mechanism of interest to the aeroelasticity community. The main objective is to show how the spatial-temporal decomposition approach can be used to enhance our understanding on the underlying physics.

### 7.1. Tip clearance flow

In the first example, the Hilbert transform-based spatial-temporal analysis is used to investigate the aeroelastic effects of the complex tip clearance flows in a three-dimensional oscillating compressor cascade in bending mode. While the adverse impact of tip clearance flow on the compressor aerodynamic performance is widely recognized [32], its aeroelastic effects are not well understood. The experiment [26] and the computation [6] of the oscillating compressor cascade showed a destabilizing impact of the tip clearance. Dong et al. [33] had a similar observation from the wide-chord transonic fan vibrating in the bending mode. On the other hand, Besem and Kielb [34] reported a non-monotonic variation of aerodynamic damping with tip clearance size. The damping initially increased until reaching a maximum then decreased when the tip gap increased. In contrast, Fu et al. [35] showed that the aerodynamic damping initially decreased until reaching a minimum then increased with a larger tip gap. Thus, the influence of tip clearance on the aerodynamic damping still remains inconclusive, which receives more attention recently thanks to a more affordable 3D flutter prediction routine.

The simulation method adopted here is decoupled, thus the computational results can still be analyzed using the conventional energy method. We will show that the Hilbert transform-based approach is not only consistent with the conventional energy method when applied to the decoupled scenario but also complements the findings from the decoupled approach. At first, the analyzed unsteady pressure responses at the 95% spanwise location are compared between the two methods, as shown in Fig. 4. The perfect match between the conventional energy method and the Hilbert transform-based approach confirms the consistency of the proposed approach when applied to the common decoupled simulation routine. From Fig. 4, the high unsteady pressure amplitude on the rear part of the suction surface is due to the impact of the tip clearance flow, which travels across the tip gap from the pressure surface to the suction surface. The phase distribution is closely related to the aerodynamic damping, thus its drastic difference compared to the front part of the suction surface is of interest.

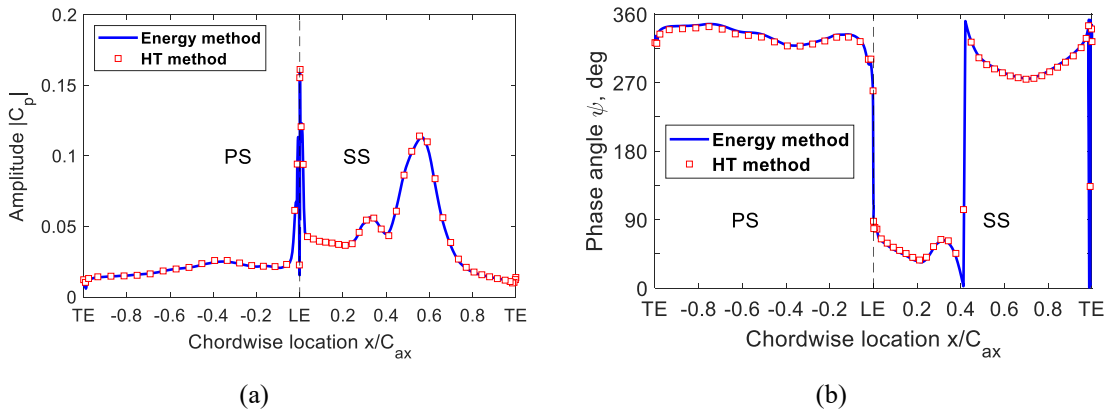


**Fig. 4.** Comparison between the energy method and the Hilbert transform-based method on the analysis of unsteady pressure responses at 95% span: (a) Amplitude and (b) Phase distribution.

To identify the underlying mechanism behind the observed destabilizing effect, we shall study the time-averaged damping distribution on blade surfaces. The suction surface is of particular interest due to notable events taking place when the tip gap is enlarged (see Fig. 3 and Fig. 4). Fig. 5 compares the local damping distribution at two sizes of tip clearance configuration. There are two distinctive regions that attract our immediate attention:

- The front part near the leading edge (denoted as part **A**). It stretches from the leading edge to about 30% to 40% axial chord. This region exists in the majority of spanwise location, although it seems to be more pronounced near tip. Part **A** shows a strong stabilizing effect with positive sign of aerodynamic damping.
- The rear part (denoted as part **B**). This part takes place aft the formation of part **A** and covers the rest of axial chord position. The region is however confined to near tip. Part **B** shows a destabilizing effect with negative

sign of aerodynamic damping. It can also be observed that the size and strength of part **B** increase at a larger tip gap configuration.

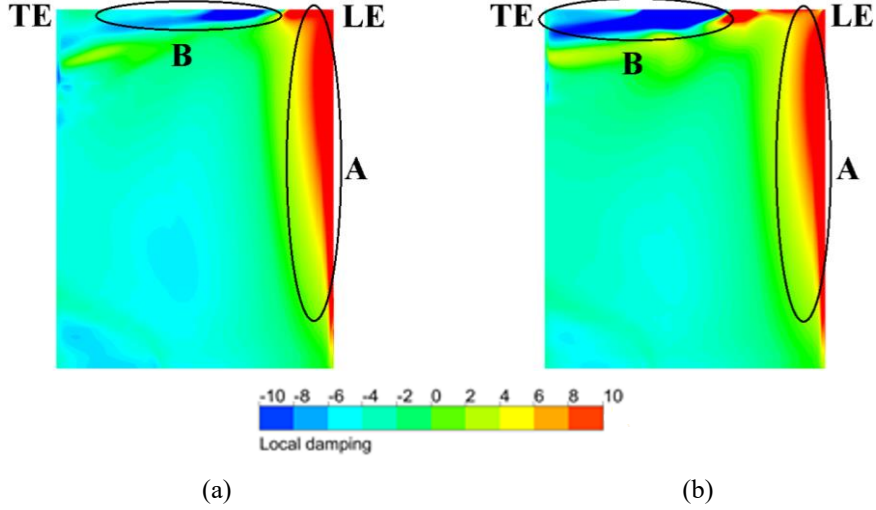


**Fig. 5.** Local damping distribution on the blade suction surface at: (a) 1% tip gap and (b) 2% tip gap.

The front part **A** can be regarded to be largely independent of the tip gap since the affected area exists at low radial location near hub. A quasi-steady model is proposed to explain the characteristic of part **A**. More importantly, the Hilbert transform-based spatial-temporal aerodynamic damping will be used to complement the quasi-steady model as the objective of the current work.

Consider a sinusoidal vibration normal to the blade chord:

$$y = \hat{y}\sin(\omega t) \quad (36)$$

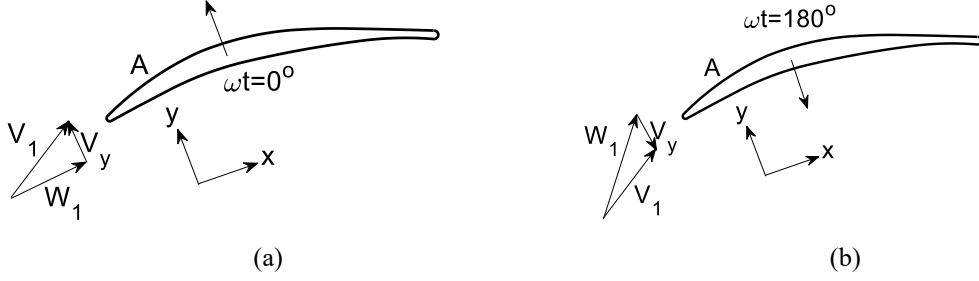
The pressure forces on the blade pressure surface and suction surface contributes oppositely to the blade lift:

$$f = f_{PS} + f_{SS} \quad (37a)$$

$$f_{PS} = \widehat{f_{PS}}\sin(\omega t + \psi_{PS}) \quad (37b)$$

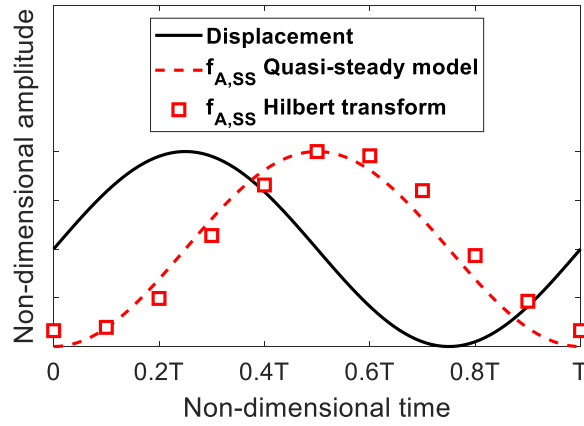
$$f_{SS} = -\widehat{f_{SS}}\sin(\omega t + \psi_{SS}) \quad (37c)$$

At  $\omega t = 0^\circ$ , the blade is going to move in the positive y-direction with a vibratory velocity  $V_y$ . Given the absolute inflow velocity  $V_1$ , the velocity diagram (Fig. [6a]) gives a relative velocity  $W_1$ . This situation reduces the effective incidence angle felt by the blade. Therefore, the blade loading at the leading edge will reduce, leading to a higher local pressure on the suction surface. This instantaneous increase in local pressure on the suction surface contributes to a reduction in blade lift in the positive y-direction. Similarly, it can be argued that the positive incidence effect would happen at  $\omega t = 180^\circ$  (Fig. [6b]), where the blade is subject to a vibratory velocity  $V_y$  in the negative y-direction. At this instant, the blade loading at the leading edge will increase, leading to a reduction in local pressure on the suction surface. In overall, the force on the suction surface should have a phase angle  $\psi_{SS} = 90^\circ$ . Part **A** is thus stabilizing since  $\Xi_{SS} \propto \sin(\psi_{SS})$  (i.e. positive increase in lift force opposing to the motion). The quasi-steady behavior of the blade loading due to the change of effective incidence angle has also been observed in a previous work, where the blades are arbitrarily mis-staggered but their blades are closely related to the mis-staggering pattern (Ref. [36]).



**Fig. 6.** Quasi-steady model for the leading edge incidence effect (for front part **A**): (a) Negative incidence and (b) Positive incidence effect.

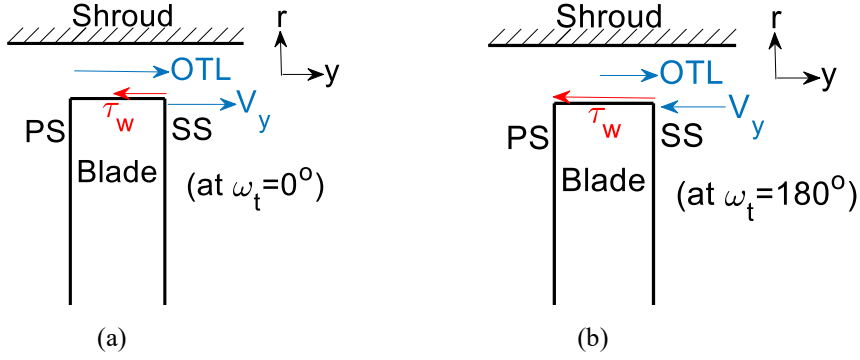
Fig. 7 compares the temporal evolution of the force induced by the movement of the suction surface  $f_{A,SS}$  obtained from the Hilbert transform analysis to that hypothesized by the quasi-steady model. The Hilbert transform-based analysis can be seen to complement the quasi-steady model predictions.



**Fig. 7.** Comparison between quasi-steady model and Hilbert transform analysis during one period of vibration for part **A**.

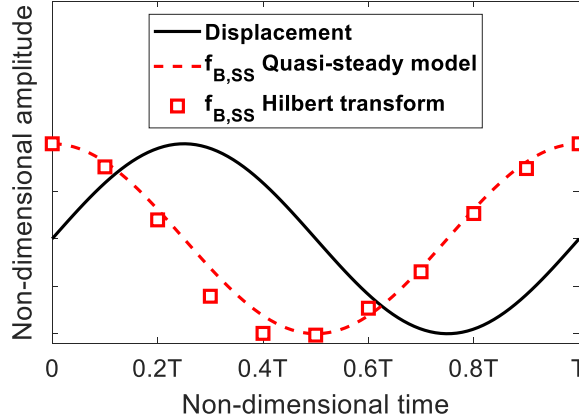
On the other hand, the rear part **B** has an evident signature of the tip leakage flow since it is confined to the limited radial location near tip. The negative aerodynamic damping characteristics of this part can also be explained using a quasi-steady model closely related to the strength of overtip leakage (OTL) flow. The tip leakage flow mechanism is driven due to the pressure difference between the blade suction and pressure surfaces. The flow would spill from the pressure surface towards the suction surface through the tip clearance. During this process, the overtip leakage flow is resisted by the shear stresses from the blade tip and shroud surfaces. In the present context, we shall focus on the blade tip wall shear stresses.

Fig. 8a shows the axial cut of the blade through part **B**. At  $\omega t = 0^\circ$ , the blade tip has a vibratory velocity  $V_y$  in the positive  $y$ -direction. Considering the blade tip surface, an increase in the surface velocity leads to a reduction of velocity gradient in the radial direction  $dV/dr$  in the tip gap, and thus a reduction in wall shear stress  $\tau_w \propto dV/dr$ . As a result, the overtip flow should be strongest at this instant. Recalling the effects of tip leakage flow on the blade surfaces' pressure distribution (see Fig. 3), a stronger tip leakage flow corresponds to an increase in blade loading at region B. Regarding Fig. 8b, it is the instant ( $\omega t = 180^\circ$ ) at which the overtip flow is weakest due to an increase in wall shear stress  $\tau_w$ . Thus, the blade loading is minimum at this point. In overall, the lift force contribution from the suction surface should have a phase angle  $\psi_{SS} = -90^\circ$ . Hence, part **B** has a destabilizing aeroelastic effect.



**Fig. 8.** Quasi-steady model for the overtip leakage flow effect (for rear part **B**): (a) Strong tip leakage flow and (b) Weak tip leakage flow effect.

Using the Hilbert transform-based analysis method, the temporal evolution of blade loading on the suction surface at part **B** is plotted in Fig. 9. Again, it can be seen that the Hilbert transform analysis can contribute to the validation of the proposed quasi-steady model to improve understanding of the destabilizing effects due to overtip leakage flow.



**Fig. 9.** Comparison between quasi-steady model and Hilbert transform analysis during one period of vibration for part **B**.

In Fig. 10, a further comparison between two tip gap size configurations at 95% spanwise location is presented. It can be seen that most changes are localized on the rear part of the suction surface (part **B**), while the pressure surface remains almost unaffected. After 50% chord, both configurations have phase angles of roughly  $\psi_{SS} = 270^\circ$  (or  $\psi_{SS} = -90^\circ$ ), in line with the previous discussion regarding the quasi-steady model. In addition, the amplitude of large tip gap configuration (i.e. TipC = 2%) increases dramatically in this region. Therefore, a large tip gap would induce a more significant destabilizing zone, which in turn decreases the overall aerodynamic stability.

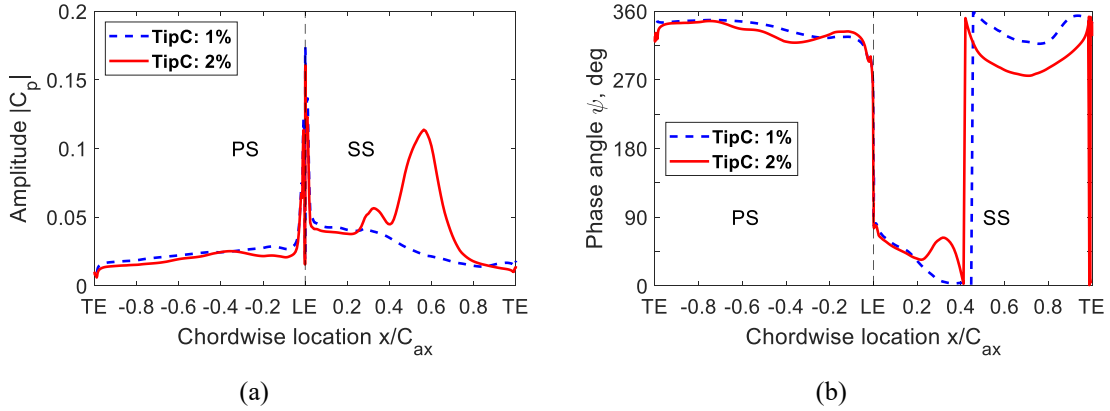
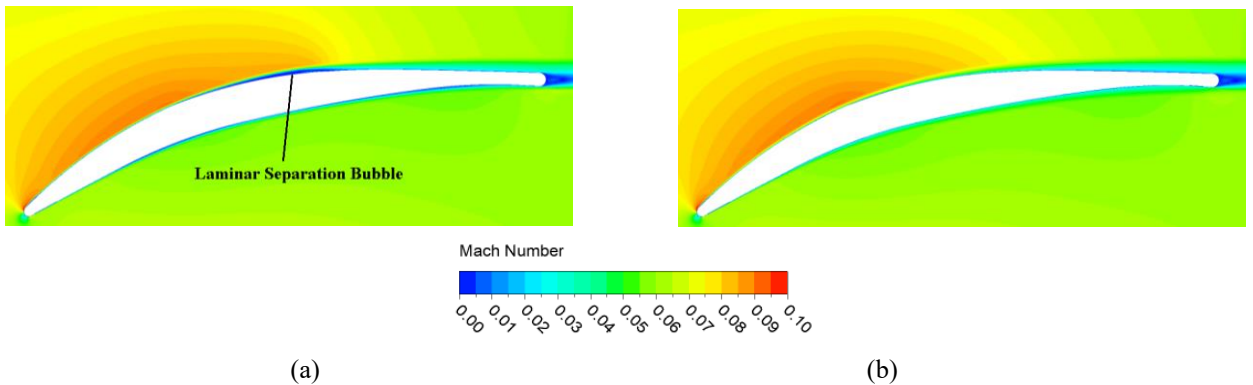


**Fig. 10.** Unsteady pressure responses of two tip gap size configurations at 95% spanwise location: (a) Amplitude and (b) Phase distribution.

## 7.2. Transitional flow with laminar separation bubble

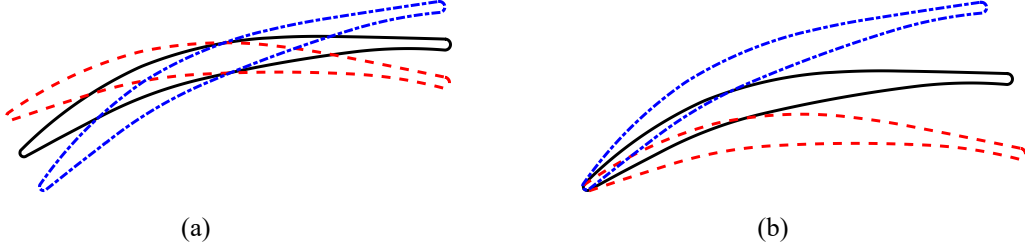
In the next example, the Hilbert transform-based analysis approach is adopted to investigate the influence of the laminar separation bubble on the aeroelastic stability. This phenomenon takes place in transitional flow condition, typically at low Reynolds number, which is strongly relevant to low-speed and/or high-altitude UAV applications. Although the aerodynamics and aerothermal effects of transitional flow are widely studied for both compressors and turbines [27-30, 37], the investigation of its aeroelastic characteristics is rare in the literature. In computational aeroelasticity, fully-turbulent URANS model is commonly used due to its simplicity and robustness. Unless a high fidelity model such as LES or hybrid RANS/LES is used, the common URANS turbulence model is unable to capture the transitional effects. To overcome this issue and improve the transitional flow prediction at a modest cost, a variety of transitional flow models are developed and extended from the common turbulence model [31, 38]. However, the transitional URANS turbulence model is still more expensive compared to the fully-turbulent model because more transport equations need to be solved and the mesh requirement is more demanding. Thus, the use of transition model in computational aeroelasticity has not been common.

Adopting the same flow condition and mesh resolution, two computations with fully-turbulent and transitional models are used to contrast the aeroelastic effects of the laminar separation bubble. Fig. 11 shows the steady Mach number contours of the computational prediction with fully-turbulent and transitional models. A mid-chord separation bubble can clearly be observed in the transitional model (Fig. 11a), while the flow is smooth in fully-turbulent computation (Fig. 11b).



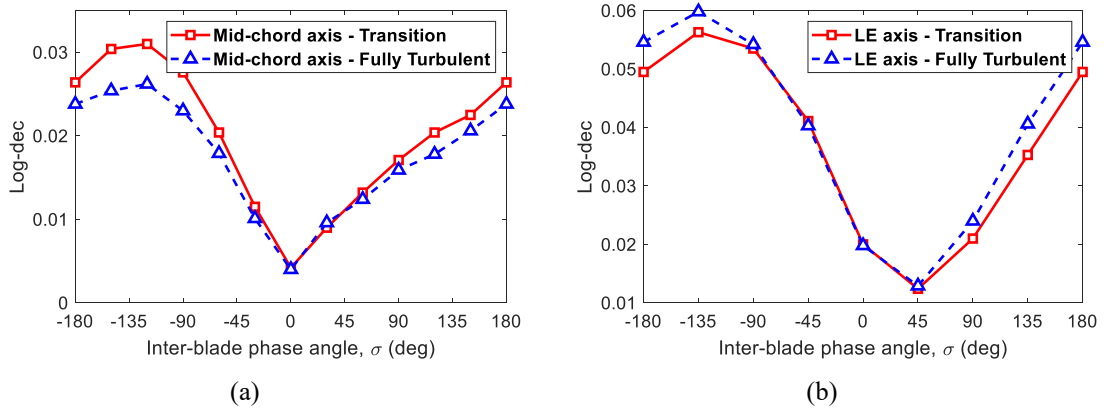
**Fig. 11.** Mid-span steady Mach number contour predicted by: (a) Transitional and (b) Fully-turbulent model.

The vibration mode chosen in this example is torsional and the simulation method is fully-coupled. In addition, two locations of the torsion axis, namely mid-chord and leading edge, will be examined. This would help to improve understanding of the relative aeroelastic effects of the mid-chord laminar separation bubble. Since the unsteady moment acting on the oscillating blade is proportional to its moment arm with respect to the location of the torsion axis, it is initially suspected that the leading edge torsion axis would have a more pronounced effect of the laminar separation bubble compared to that with the mid-chord torsion axis. Fig. 12 illustrates the displacement of the oscillating cascade during the vibration period with different torsion axis locations.



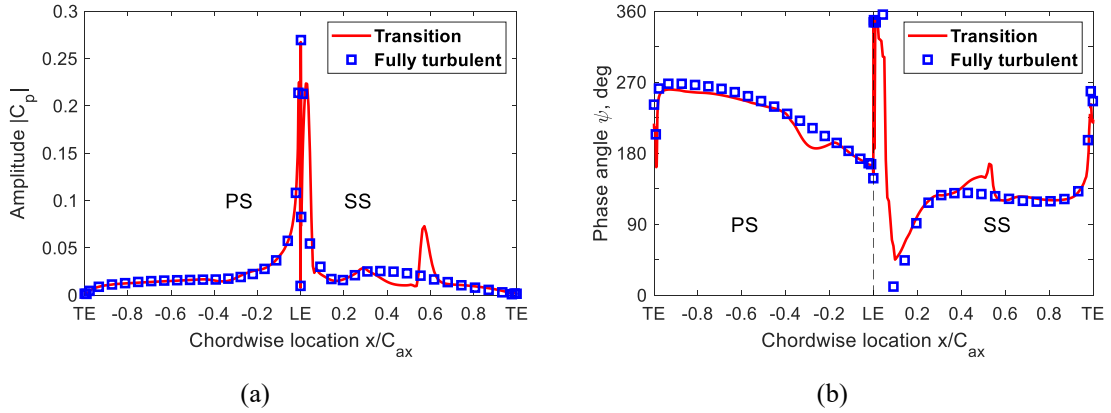
**Fig. 12.** Illustration of torsion mode vibration at different torsion axis locations: (a) Axis at mid-chord and (b) Axis at leading edge.

Fig. 13a presents the overall log-dec for the vibration of mid-chord torsion axis, while Fig. 13b shows that for the vibration of leading edge torsion axis. Both figures compare the prediction between the transitional and fully-turbulent models. It can be seen that the predicted overall log-dec of two turbulence models have a similar trend. Interestingly, the difference among two configurations is almost negligible at the minimum stability point. It is known that if the blade experiences flutter, it will couple to neighbor blades to vibrate at the minimum stability point with the corresponding inter-blade phase angle. Thus, accurate prediction of this minimum damping point is of strong interest.



**Fig. 13.** Overall log-dec curves for different torsion axis locations turbulence models: (a) Axis at mid-chord and (b) Axis at leading edge.

We will further examine in detail the minimum stability inter-blade phase angle conditions predicted by the transitional and fully-turbulent models. Firstly, Fig. 14 presents the unsteady pressure responses predicted at IBPA 0deg for the vibration with the mid-chord torsion axis. One is reminded that the local unsteady pressure amplitudes and phases reported in this section are time-averaged across a fully-coupled vibration period using the Hilbert transform-based analysis method. From Fig. 14, it is clear that the two turbulence models predict almost the same responses on the blade pressure surface. However, distinct features on the suction surface can be observed. Around mid-chord, the transitional results show a spike in the unsteady pressure amplitude and phase, while the fully-turbulent flow remains smooth. Nevertheless, the extent of this influenced zone is restrictive compared to the whole blade surfaces, leading to a minimal overall impact induced by the separation bubble.



**Fig. 14.** Unsteady pressure responses at IBPA 0deg with mid-chord torsion axis: (a) Amplitude and (b) Phase distribution.

Next, Fig. 15 shows the unsteady pressure responses predicted at IBPA +45deg for the vibration with the leading edge torsion axis. Similarly to the previous case of mid-chord torsion axis, a spike of amplitude is observed on the suction surface in the transitional flow condition, while the pressures surface is not affected. The phase even changes its sign in this region around mid-chord (Fig. 15b). However, these contrast local dissimilarities eventually cancelled out to produce a negligible difference in the overall damping, even in the case of leading edge torsion axis where the moment induced by the mid-chord separation bubble is larger. As a result, the mid-chord laminar separation bubble is deemed to have an almost negligible effect on the overall aeroelastic stability. This finding is in agreement with what has been observed from previous experimental [26, 39] and computational [6, 40] results.

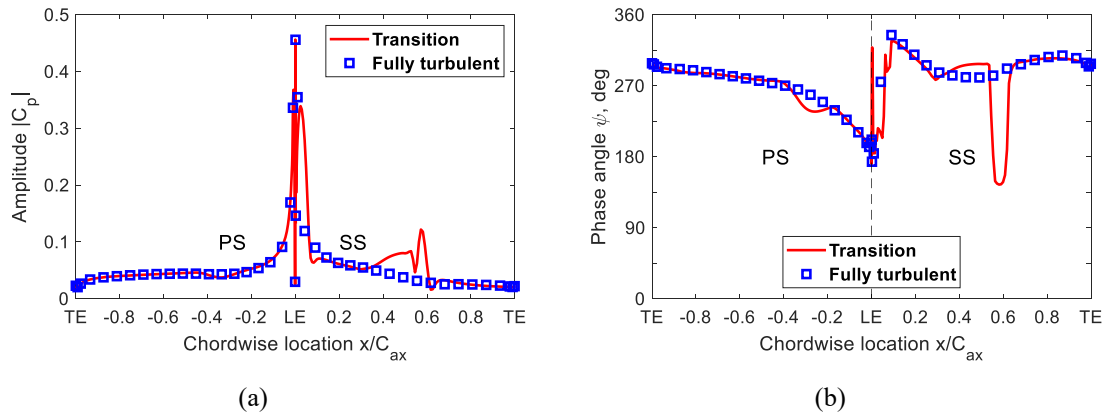


**Fig. 15.** Unsteady pressure responses at IBPA +45deg with leading edge torsion axis: (a) Amplitude and (b) Phase distribution.

### 7.3. Stall flutter

In the last example, the Hilbert transform-based method is adopted to study stall flutter. Stall flutter is the aeroelastic stability problem that typically happens at off-design condition (i.e. near stall) when the incidence angle is high. To simulate the stall flutter phenomenon, the flow angle is iteratively increased until a significant separation is observed at the rear of the blade suction surface. Fig. 16 shows the steady Mach number contour at the stall flow condition. There is a small separation bubble near the leading edge followed by flow reattachment. On the other hand, the separation at the rear of the suction surface no longer attaches (i.e. open separation bubble). The normalized chordwise positions  $x/C_{ax} = 0.5, 0.6$ , and  $0.7$  are plotted for reference. The flow is still attached at  $x/C_{ax} = 0.5$ . The separation happens around  $x/C_{ax} = 0.6$  and the flow is fully separated downstream.

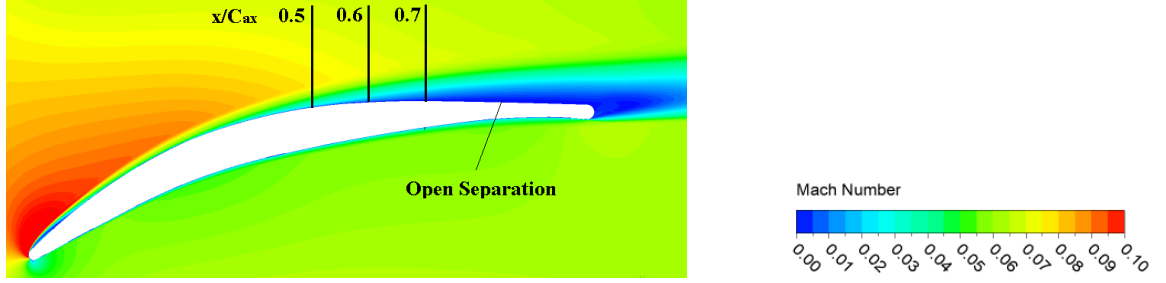


**Fig. 16.** High-incidence configuration Mach number contour.

Fig. 17 presents the local unsteady pressure responses on the blade surfaces. The local amplitudes and phases are time-averaged across the vibration period. From the amplitude plot (Fig. 17a), it can be seen that the leading-edge separation bubble induces a significant spike on the suction surface, while the amplitudes remain relatively low for the rear part even at the open separation bubble region. On the other hand, the phase plot (Fig. 17b) shows a clear jump in phase angle distribution around  $x/C_{ax} = 0.1$  and  $0.6$ . The former dictates the location of small leading edge separation bubble, while the latter represents the transition point of the open separation bubble.

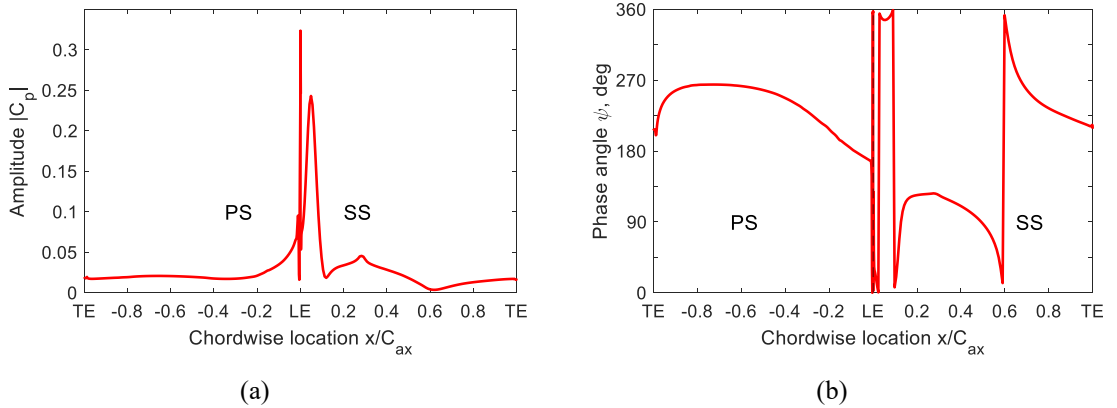


**Fig. 17.** Unsteady pressure responses at stall condition: (a) Amplitude and (b) Phase distribution.

Our interest shifts to the behavior around the transition point of the open separation bubble on the suction surface. Fig. 18 presents the temporal evolution of the local aerodynamic damping for different points on the blade suction surface around the open separation bubble during two successive vibration periods. It can be observed that the local part of the airfoil upstream the transition point ( $x/C_{ax} = 0.53$ ) is stable. On the other hand, the part downstream the transition point ( $x/C_{ax} = 0.7$ ), well inside the flow recirculation region, is unstable. In between there is the transition point ( $x/C_{ax} = 0.7$ ), where the aerodynamic damping is alternately positive (stable) and negative (unstable) during the vibration period. Unlike the previous example where the separation bubble quickly reattaches and contributes insignificantly to the overall aeroelastic stability, the large open separation in the stall condition leads to a greater contribution to the instability. Therefore, it can be concluded that the formation of the open separation bubble and its size are closely related to the onset of stall flutter.

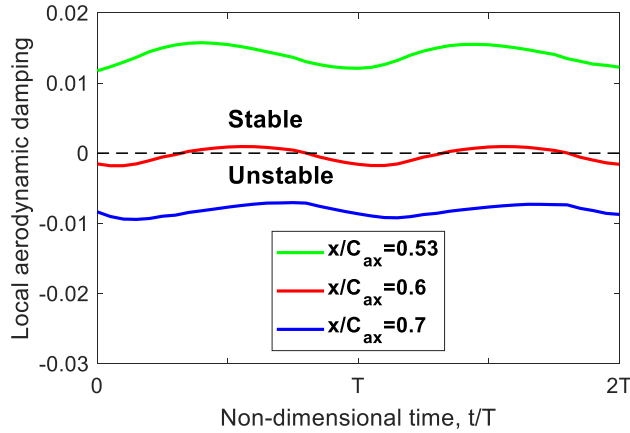


Fig. 18. Temporal evolution of the local aerodynamic damping around the open separation bubble.

## 8. Conclusions

Accurate and efficient numerical predictions of flutter is essential for the turbomachinery industry. However, use of the common decoupled numerical method is no longer desirable due to a number of factors such as the pursuit of a low mass ratio/low stiffness material and an innovative propulsion architecture. Hence, adoption of the fully-coupled method is expected to grow in the near future. While the fully-coupled method is more computational demanding, it has not been used effectively to improve understanding of the physical vibration mechanisms because the global parameter logarithmic decrement is typically used to judge the aeroelastic stability. The current work addresses this challenge by developing a spatial-temporal analysis approach based on the Hilbert transform. The proposed approach is suitable for non-linear non-stationary data obtained from the fully-coupled method. Interestingly, it is designed to be consistent with the well-known energy method when applying to the decoupled simulation data.

The Hilbert transform-based analysis approach is adopted in three computational examples to show how the new method could elucidate the vibration mechanisms. The findings of each example are summarized below:

- 1) Tip clearance flow has a destabilizing effect on the compressor aeroelastic stability. The rear part of the suction surface contributes most to the destabilization.
- 2) Mid-chord laminar separation bubble induces fluctuation of local aerodynamic damping on the suction surface. However no significant impact on the overall damping is observed at the minimum stability point. The observation is consistent for both mid-chord and leading edge torsion axis vibration pattern.
- 3) A large open separation bubble near the trailing edge is observed in the stall flow condition (i.e. high flow incidence angle). Before the formation of the separation bubble, the compressor blade is locally stable. Around the transition point, the local aerodynamic damping fluctuates around zero, which interchanges continuously between the stable and unstable zone. After the transition point, the blade is locally unstable in a well-developed open separation bubble.

## Acknowledgements

The support from the EPSRC CDT in Gas Turbine Aerodynamics and the Chair of Computational Aerothermal Engineering Bursary are much appreciated. The author would like to thank Prof. Li He for his continuous support and suggestion.

## Appendix A.

If the vibration is periodic as in the decoupled method, the phase difference  $\psi$  between the blade response and the blade motion can be regarded as a constant. The cycle-averaged work done during the period  $T$  becomes:

$$\begin{aligned} W_d &= \int_t^{t+T} W_d(t) dt \\ &= \int_t^{t+T} \hat{f} \omega \hat{q} \cdot \sin \psi \cdot \cos(\omega t)^2 dt \end{aligned} \quad (\text{A1})$$

We also note that  $\int_t^{t+T} \cos(\omega t)^2 dt = \pi/\omega$ .

The cycle-averaged work done in Eq. A1 becomes:

$$W_d = -\pi \hat{f} \hat{q} \sin \psi \quad (\text{A2})$$

The cycle-averaged aerodynamic damping can be calculated as below, which is consistent with the conventional energy method as in Eq. 6:

$$\Xi = \frac{-\pi \hat{f} \hat{q} \cdot \sin(\psi)}{(P_{01} - P_2) \widehat{q_{tip}}^2} = \frac{1}{C} \int_s \frac{-\pi \hat{p} \hat{q} \cdot \sin(\psi) ds}{(P_{01} - P_2) \widehat{q_{tip}}^2} \quad (\text{A3})$$

## References

- [1] Lane, F., 1956, "System Mode Shapes in the Flutter of Compressor Blade Rows," *Journal of the Aeronautical Sciences*, 23(1), pp. 54-66. doi.org/10.2514/8.3502
- [2] Carta, F. O., 1967, "Coupled Blade-Disk-Shroud Flutter Instabilities in Turbojet Engine Rotors," *Journal of Engineering for Gas Turbines and Power*, 89(3), pp. 419-426. doi.org/10.1115/1.3616708
- [3] Marshall, J. G., and Imregun, M., 1996, "A Review of Aeroelasticity Methods with Emphasis on Turbomachinery Applications," *Journal of Fluids and Structures*, 10(3), pp. 237-267. doi.org/10.1006/jfls.1996.0015
- [4] Huang, X., He, L., and Bell, D. L., 2009, "Experimental and Computational Study of Oscillating Turbine Cascade and Influence of Part-Span Shrouds," *Journal of Fluids Engineering*, 131(5), p. 051102. doi.org/10.1115/1.3111254
- [5] Vahdati, M., and Cumpsty, N., 2016, "Aeroelastic Instability in Transonic Fans," *Journal of Engineering for Gas Turbines and Power*, 138(2), p. 022604. doi.org/10.1115/1.4031225
- [6] Phan, H. M., and He, L., 2020, "Validation Studies of Linear Oscillating Compressor Cascade and Use of Influence Coefficient Method," *Journal of Turbomachinery*, 142(5), p. 051005. doi.org/10.1115/1.4045657
- [7] Castanier, M. P., and Pierre, C., 2006, "Modeling and Analysis of Mistuned Bladed Disk Vibration – Current Status and Emerging Directions," *Journal of Propulsion and Power*, 22(2), pp. 384-396. doi.org/10.2514/1.16345
- [8] Brandstetter, C., Duquesne, P., Paoletti, B., Aubert, S., and Ottavy, X., 2019, "Project PHARE-2 – A High-Speed UHBR Fan Test Facility for a New Open-Test Case," *Journal of Turbomachinery*, 141(10), p. 101004. doi.org/10.1115/1.4043883
- [9] Rendu, Q., Aubert, S., and Ferrand, P., 2020, "Numerical Identification of Mechanisms Triggering 2D Choke Flutter in Transonic Fan," *Journal of Fluids and Structures*, 97, p. 102879. doi.org/10.1016/j.jfluidstructs.2020.102879
- [10] Provenza, A. J., Duffy, K. P., and Bakhle, M. A., 2019, "Aeromechanical Response of a Distortion-Tolerant Boundary Layer Ingesting Fan," *Journal of Engineering for Gas Turbines and Power*, 141(1), p. 011011. doi.org/10.1115/1.4040739
- [11] Stapelfeldt, S. C., Parry, A. B., and Vahdati, M., 2016, "Investigation of Flutter Mechanisms of a Contra-Rotating Open Rotor," *Journal of Turbomachinery*, 138(5), p. 051009. doi.org/10.1115/1.4032186
- [12] Sadeghi, M., and Liu, F., 2005, "Computation of Cascade Flutter by Uncoupled and Coupled Methods," *International Journal of Computational Fluid Dynamics*, 19(8), pp. 559-569. doi.org/10.1080/10618560500508367
- [13] Carstens, V., and Belz, J., 2001, "Numerical Investigation of Nonlinear Fluid-Structure Interaction in Vibrating Compressor Blades," *Journal of Turbomachinery*, 123(2), pp. 402-408. doi.org/10.1115/1.1354138
- [14] Chahine, C., Verstraete, T., and He, L., 2019, "A Comparative Study of Coupled and Decoupled Fan Flutter Prediction Methods under Variation of Mass Ratio and Blade Stiffness," *Journal of Fluids and Structures*, 85, pp. 110-125. doi.org/10.1016/j.jfluidstructs.2018.12.009

- [15] Vahdati, M., Simpson, G., and Imregun, M., 2011, "Mechanisms for Wide-Chord Fan Blade Flutter," *Journal of Turbomachinery*, 133(4), p. 041029. doi.org/10.1115/1.4001233
- [16] Gan, J., Im, H. S., Espinal, D., Lefebvre, A., and Zha, G. C., 2014, "Investigation of a Compressor Rotor Non-Synchronous Vibration with and without Fluid-Structure Interaction," ASME Paper No. GT2014-26478. doi.org/10.1115/GT2014-26478
- [17] Phan, H. M., and He, L., 2021, "Investigation of Mistuned Oscillating Cascade Using Fully-Coupled Method," ASME Paper No. GT2021-59124.
- [18] Phan, H. M., and He, L., 2021, "Analysis of Structurally and Aerodynamically Mistuned Oscillating Bladerow Using Fully-Coupled Method," GPPS Paper No. GPPS-TC-2021-330.
- [19] Kim, Y., and Park, M. J., 2015, "Identification of the Nonlinear Roll Damping and Restoring Moment of a FPSO Using Hilbert Transform," *Ocean Engineering*, 109, pp. 381-388. doi.org/10.1016/j.oceaneng.2015.09.019
- [20] Chen, B., Zhao, S. L., and Li, P. Y., 2014, "Application of Hilbert-Huang Transform in Structural Health Monitoring: A State-of-the-Art Review," *Mathematical Problems in Engineering*. doi.org/10.1155/2014/317954
- [21] Zhao, Y., Zhang, B., Han, F., Tian, H., Yu, X., and Zhu, J., 2018, "Instantaneous Characteristics of Nonlinear Torsion Pendulum and Its Application in Parameter Estimation of Nonlinear System," *Mathematical Problems in Engineering*. doi.org/10.1155/2018/7858403
- [22] Bowles, P. O., Corke, T. C., Coleman, D. G., Thomas, F. O., and Wasikowski, M., 2014, "Improved Understanding of Aerodynamic Damping Through the Hilbert Transform," *AIAA Journal*, 85, pp. 110-125. doi.org/10.2514/1.J052630
- [23] Malik, W., and Raveh, D. E., 2020, "Aerodynamic Damping Investigations of Light Dynamic Stall on a Pitching Airfoil via Modal Analysis," *Journal of Fluids and Structures*, 98, p. 103111. doi.org/10.2514/1.J052630
- [24] Jacobson, K. E., Kiviahio, J. F., Kennedy, G. J., and Smith, M. J., 2019, "Evaluation of Time-Domain Damping Identification Methods for Flutter-Constrained Optimization," *Journal of Fluids and Structures*, 87, pp. 174-188. doi.org/10.1016/j.jfluidstructs.2019.03.011
- [25] Feldman, M., 2011, "Hilbert Transform in Vibration Analysis," *Mechanical Systems and Signal Processing*, 25(3), pp. 735-802. doi.org/10.1016/j.ymssp.2010.07.018
- [26] Yang, H., and He, L., 2004, "Experimental Study on Linear Compressor Cascade with Three-Dimensional Blade Oscillation," *Journal of Propulsion and Power*, 20(1), pp. 108-188. doi.org/10.2514/1.1280
- [27] Cumpsty, N. A., Dong, Y. Y., and Li, Y. S., 1995, "Compressor Blade Boundary Layers in the Presence of Wakes," ASME Paper No. 95-GT-443. doi.org/10.1115/95-GT-443
- [28] Halstead, D. E., Wisler, D. C., Okiishi, T. H., Walker, G. J., Hodson, H. P., and Shin, H. W., 1997, "Boundary Layer Development in Axial Compressors and Turbines: Part 2 of 4-Compressors," *Journal of Turbomachinery*, 119(3), pp. 426-444. doi.org/10.1115/1.2841142
- [29] Brunner, S., Fottner, L., and Schiffer, H. P., 2000, "Comparison of Two Highly Loaded Low Pressure Turbine Cascades Under the Influence of Wake-Induced Transition," ASME Paper No. 2000-GT-0268. doi.org/10.1115/2000-GT-0268
- [30] Stieger, R. D., and Hodson, H. P., 2004, "The Transition Mechanism of Highly Loaded Low-Pressure Turbine Blades," *Journal of Turbomachinery*, 126(4), pp. 536-543. doi.org/10.1115/1.1773850
- [31] Menter, F. R., Langtry, R. B., Likki, S. R., Suzen, Y. B., Huang, P. G., and Völker, S., 2006, "A Correlation-Based Transition Model Using Local Variables – Part I: Model Formulation," *Journal of Turbomachinery*, 128(3), pp. 413-422. doi.org/10.1115/1.2184352
- [32] Storer, J. A., and Cumpsty, N. A., 1991, "Tip Leakage Flow in Axial Compressors," *Journal of Turbomachinery*, 113(2), pp. 252-259. doi.org/10.1115/1.2929095
- [33] Dong, X., Zhang, Y., Zhang, Z., Lu, X., and Zhang, Y., 2020, "Effect of Tip Clearance on the Aeroelastic Stability of a Wide-Chord Fan Rotor," *Journal of Engineering for Gas Turbines and Power*, 142(9), p. 091010. doi.org/10.1115/1.4048020
- [34] Besem, F. M., and Kielb, R. E., 2017, "Influence of the Tip Clearance on a Compressor Blade Aerodynamic Damping," *Journal of Propulsion and Power*, 33(1), pp. 227-233. doi.org/10.2514/1.B36121
- [35] Fu, Z., Wang, Y., Jiang, X., and Wei, D., 2015, "Tip Clearance Effects on Aero-Elastic Stability of Axial Compressor Blades," *Journal of Engineering for Gas Turbines and Power*, 137(7), p. 071009. doi.org/10.1115/1.4028019
- [36] Phan, H. M., and He, L., 2020, "Efficient Steady and Unsteady Flow Modeling for Arbitrarily Mis-Staggered Bladerow Under Influence of Inlet Distortion," *Journal of Engineering for Gas Turbines and Power*, 137(1), p. 012501. doi.org/10.1115/1.4050364
- [37] Phan, H. M., Duan, P. H., and Dinh, C. T., 2020, "Numerical Aero-Thermal Study of High-Pressure Turbine Nozzle Guide Vane: Effects of Inflow Conditions," *Physics of Fluids*, 32(3), p. 034111. doi.org/10.1063/1.5144418
- [38] Walters, D. K., and Cokljat, D., 2008, "A Three-Equation Eddy-Viscosity Model for Reynolds-Averaged Navier-Stokes Simulations of Transitional Flow," *Journal of Fluids Engineering*, 130(12), p. 121401. doi.org/10.1115/1.2979230
- [39] He, L., 1998, "Unsteady Flow in Oscillating Turbine Cascade: Part 1 - Linear Cascade Experiment," *Journal of Turbomachinery*, 120(2), pp. 262-268. doi.org/10.1115/1.2841401
- [40] He, L., 1998, "Unsteady Flow in Oscillating Turbine Cascade: Part 2 – Computational Study," *Journal of Turbomachinery*, 120(2), pp. 269-275. doi.org/10.1115/1.2841402